Geophysical Research Letters®

Key Points:

- CMIP6/DAMIP simulations show that anthropogenic signals are robustly detected for the significant wave height (H_s) trends during 1961–2020
- Greenhouse gases are the major contributor for H_s trends over the global ocean, but aerosols dominance is seen for a few regional basins
- High increase in H_s over the Polar oceans is due to greenhouse gas induced sea-ice decline, fetch enlargement and wind speed increase

Correspondence to:

A. Patra, G. Dodet and S.-K. Min,
apatra@ifremer.fr;
aninditapatra699@gmail.com;
guillaume.dodet@ifremer.fr;
skmin@postech.ac.kr

Quantifying Anthropogenic Influences on Global Wave Height Trend During 1961–2020 With Focus on Polar Ocean

Anindita Patra[1] , **Guillaume Dodet[1]** , **Seung-Ki Min[2]** , and **Antoine Hochet[1]**

[1]Laboratoire d'Océanographie Physique et Spatiale, Univ Brest CNRS IRD Ifremer, Brest, France, [2]Division of Environmental Science and Engineering, Pohang University of Science and Technology, Pohang, South Korea

Abstract This study investigates the contribution of external forcings on global and regional ocean wave height change during 1961–2020. Historical significant wave height (H_s) produced for different CMIP6 external forcings and preindustrial control conditions following the Detection and Attribution Model Intercomparison Project (DAMIP) are employed. The internal variability ranges are compared with different external forcing scenario. Statistically significant linear trends in H_s computed over regional ocean basins are found to be mostly associated with anthropogenic forcings: greenhouse gas-only (GHG) and aerosol-only (AER) forcing. For H_s, GHG signals are robustly detected and dominant for most of the global ocean, except over North pacific and South Atlantic, where AER signals are dominant. These results are supported by multi-model analysis for wind speed. The remarkable increase in H_s over the Arctic (22.3%) and Southern (8.2%) Ocean can be attributed to GHG induced sea-ice depletion and larger effective fetch along with wind speed increase.

Plain Language Summary We quantify the influence of anthropogenic forcings (greenhouse gas-only and aerosol-only forcing) and natural forcing to the significant wave height trends during 1961–2020 using CMIP6 individual forcing experiments. It is shown that anthropogenic influence is majorly responsible for the significant wave height changes and natural (solar and volcanic activities) forcings show limited influence. The human-induced greenhouse gas increases are found to be the dominating factor for most of the global ocean, whereas anthropogenic aerosols are the dominating forcing for a few ocean basins, such as North Pacific and South Atlantic. The multimodel analysis for wind speed corroborates the relative dominance of signals in wave height change. In the polar ocean (Arctic and Southern Ocean), we see exceptional wave height increase compared to other regions. Sea-ice decline associated with greenhouse gas forcing provides larger fetch for the waves to grow in polar region. Moreover, the contrasting influence of greenhouse gas and aerosol forcing to sea-ice area and wind speed changes are shown to drive the total wave height changes.

1. Introduction

Wind-waves are capable of affecting continuous ocean-atmosphere exchange (Cavaleri et al., 2012), atmospheric circulation and subsequently surface winds (Chen et al., 2019), the former's driver; thus introducing a feedback loop in the global climate system. There are other ways of mutual interactions with the climate system, such as: fragmentation of ice floes in the marginal ice zone (Boutin et al., 2020), deepening of the ocean mixed layer depth due to the effect of turbulence induced by wave orbital motions (Toffoli et al., 2012), ejection of sea spray in the atmosphere and air entrainment in the water column during wave breaking (Deike, 2022). Since the industrialization, Earth's climate system has undergone some drastic changes (Masson-Delmotte et al., 2021). Being a component of the global climate system, wind-waves have experienced intensification or weakening in many regions of the global ocean (Meucci et al., 2023; Timmermans et al., 2020; Young & Ribal, 2019). Understanding long-term changes in waves is crucial for a range of socio-economic and environmental applications, such as offshore and coastal activities, coastal hazards management, and renewable energy generation.

The climate response can be interpreted as a combination of an internally unforced and an externally forced variability (Hasselmann, 1993). Anthropogenic greenhouse gases and aerosols have been identified as major external forcing for the global climate change (Bindoff et al., 2013). Moreover, detection and attribution studies have shown that aerosol influences have significantly offset the global warming induced by greenhouse gases (Gillett et al., 2021; Seong et al., 2021). It is still unclear to which extent external anthropogenic forcings (i.e., greenhouse gases and aerosols), external natural forcings (solar and volcanic activities), internal climate variability, or a combination of some these, have influenced wave climate since the pre-industrial period.

Writing – original draft: Anindita Patra, Guillaume Dodet, Seung-Ki Min, Antoine Hochet
Writing – review & editing: Anindita Patra, Guillaume Dodet, Seung-Ki Min, Antoine Hochet

The Detection and Attribution Model Intercomparison Project (DAMIP; Gillett et al., 2016), under the framework of Coupled Model Intercomparison Project (CMIP6; Eyring et al., 2016) provides a variety of external forcing experiments including GHG (greenhouse gases) only, AER (aerosols) only, and NAT (natural) only forcings. This gives the opportunity to assess the relative importance of individual forcing factors. The unforced climate variability can be estimated from preindustrial control simulations (CTL) from CMIP6 models. In this context, comparing unforced CTL variability with forced simulation from CMIP5 (Taylor et al., 2012) framework, Dobrynin et al. (2015) could detect climate change signal in wave climate simulations as early as 2010–2020 decade over various regions of global ocean, such as North Atlantic, equatorial Pacific, and Southern Ocean. Another study by Hochet et al. (2023) estimated that the date of emergence (when climate change emerges from the noise of natural climate variability) of forced variability in satellite-based wave climate data records would be after 2050 in the North Atlantic. The role of internal variability on wave height trend was evaluated by a recent study (Casas-Prat et al., 2022). Nevertheless, relative contribution of different external forcing is yet to be addressed for long-term changes in wave climate.

Nonetheless, decadal changes of the wave climate in the high latitudes are particularly affected by rapid changes of the oceanic and atmospheric conditions in polar regions, such as surface winds, currents and sea ice. For instance, as sea ice extent decreases in the Arctic, greater extent of fetch becomes available for waves to grow, and consequently larger waves provide a mechanism to sea ice break and accelerate the melting, leading to a positive feedback loop (Thomson & Rogers, 2014). The dominant influence of greenhouse gases in long-term trend of surface winds as a result of modulating meridional atmospheric circulation is reported by K. Deng et al. (2021) using CMIP6 multi-model simulations.

Here, we take advantage of newly available global historical wave data simulated by WAVEWATCH III (WW3) using winds and sea ice forcings from DAMIP (Patra et al., 2023b) to provide the first estimate of relative contribution of GHG, AER, NAT, and CTL influence on significant wave height (H_s) changes over the period 1961–2020. We also examine the role of sea ice and winds associated with different forcing scenario in the Arctic and Antarctic region.

2. Model Experiments and Analysis Method

Ocean wave data are not directly available from CMIP5/CMIP6 global climate models (GCM), hence not in the framework of DAMIP. However, Patra et al. (2023b) produced historical ocean wave climate for the 1961–2020 period, using the CMIP6 model- MRI-ESM2.0 (Yukimoto et al., 2019) as forcing to WW3 over the global ocean, following the approach of DAMIP. Global 6-hourly wave height (H_s) are available at horizontal resolution of 1.0° for preindustrial control condition (CTL) and historical experiments (ALL: natural plus all anthropogenic, GHG, AER, and NAT), each consisting of five ensemble members. The control simulation, considered as time invariant, is available for 180 years. The historical simulations were conducted by changes only in the forcing of interest, while all the other forcing were kept at preindustrial level. This is the main data set analyzed here to quantify the relative contribution from greenhouse gases, aerosols, natural forcings, and internal variability.

To confirm the reproducibility of the long-term historical changes, we use other available CMIP6-based historical wave simulations, which include WW3 simulations (Meucci et al., 2023) forced with ACCESS-CM2 (Bi et al., 2020), and EC-Earth3 (Döscher et al., 2022) GCMs and the MArine Science and NUmerical Modeling (MASNUM) wavenumber spectrum wave model (MASNUM-WAM) simulations (Song et al., 2020a) forced with FIO-ESM v2.0 (Table S1 in Supporting Information S1). It should be noted here that these simulations are available only for ALL scenario (natural plus all anthropogenic) with single ensemble member, but not for separate forcings (GHG, AER, and NAT).

For wind-speed analysis, we use multimodel data sets from CMIP6 (Eyring et al., 2016) to corroborate the patterns from multimodel mean with that of MRI-ESM2.0. Although there are many climate models participating in the CMIP6, there are only three models - namely CanESM5 (Swart et al., 2019), CNRM-CM-6-1 (Voldoire et al., 2019), and IPSL-CM6A-LR (Boucher et al., 2018) - that have at least 10 ensemble members for each of the historical experiments of DAMIP used here (Table S2 in Supporting Information S1). The daily data for wind speed from these models are interpolated to the same regular grid of 1.0° resolution. To access the robustness of trend, we identify the grids where >50% of members have statistically significant trend (at 5% level) and >80% (of the members previously identified with statistically significant trend) have the same sign for trend. In this way,
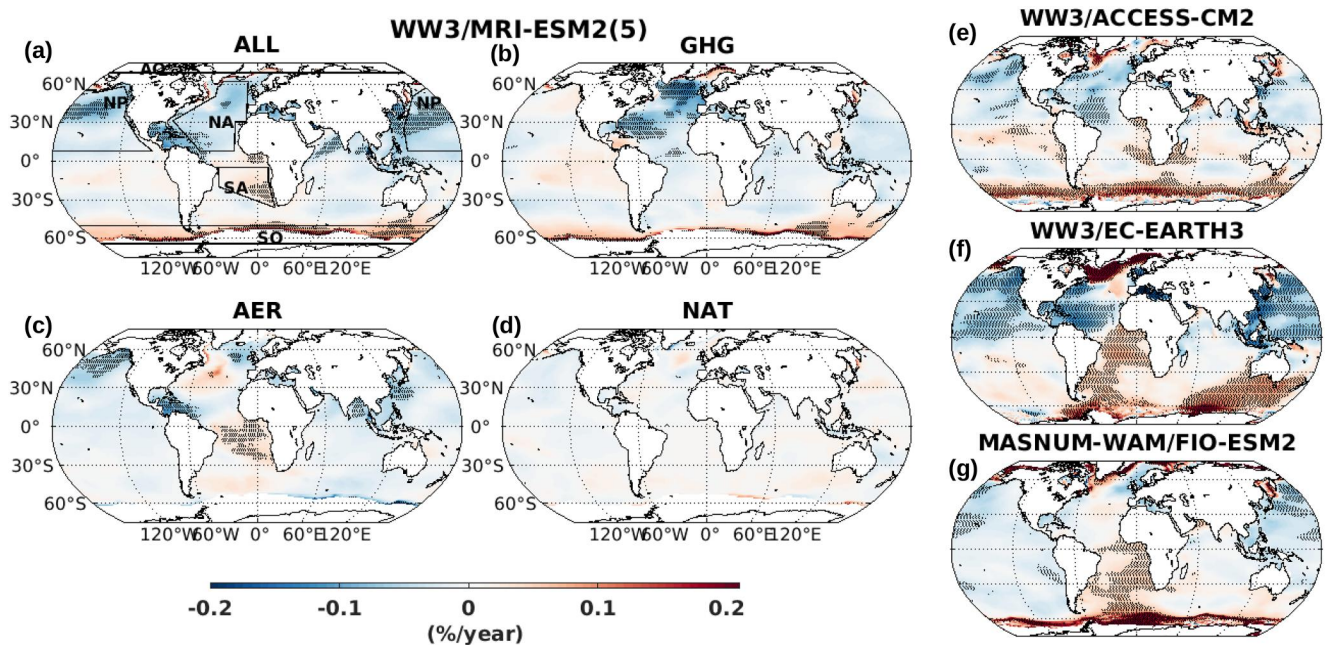
Figure 1. Linear trend (%) expressed as percentage change per year during 1961–2020 for annual mean H_s from WW3/MRI-ESM2.0 simulations for (a) ALL, (b) GHG, (c) AER, and (d) NAT forcing scenario (5 member mean). The percentage is calculated with respect to 1961–2020 climatology. Boxes (a) indicate the regions with robust change: North Atlantic (NA), South Atlantic (SA), North Pacific (NP), Southern Ocean (SO), Arctic Ocean (AO). The right side panel shows trends for historical-ALL scenario from (e) WW3/ACCESS-CM2, (f) WW3/EC-Earth3, and (g) MASNUM-WAM/FIO-ESM v2.0 (single member). All the subplots have same colorbar. Stippling designates areas of robust change (a–d) or areas of statistically significant change (t-test) for single member results (e–g). Robustness criteria accounts for both inter-annual and inter-member variability (see Methods).

the uncertainty assessment includes two types of variability: inter-member and inter-annual (Casas-Prat et al., 2024; Erikson et al., 2022; Morim et al., 2019).

We assess the 60-year linear trends in the ensemble mean H_s for ALL, GHG, AER and NAT forcings. To quantitatively compare these trends with the unforced internal variability for spatially averaged values, we apply a moving window of 60-year length in a 10-year interval to 180-year long CTL simulations. Then we compute H_s trends from each window, and take 95% confidence interval of those trends to represent the variability associated to the unforced signal.

Although ensemble averages can substantially reduce the internal climate variations, influence of internal variability can still persist due to small number of ensemble members (Deser et al., 2012). We compare the 5-year running mean H_s anomalies for each external forcing scenario during 1961–2020 with respect to the range of modeled internal variability. These are the steps followed to compute internal variability: (a) select 13 60-year-long samples from 180 year CTL simulations, (b) calculate ensemble mean of 13 time series, (c) compute 5-year running mean values of the ensemble mean (60 data points), (d) then take twice the standard deviation of the 5-year running mean time series.

In the Arctic and Antarctic Ocean, we focus on the differences between the last two decades and the first two decades of 1961–2020 for sea ice, surface wind speed and H_s. We estimate ensemble mean changes in MRI-ESM2.0 based simulations for different forcing scenario and carry out a t-test for statistical significance using 5 members × 20 years = 100 data for each period. Results over the polar ocean are computed only for grid points below sea ice threshold (0.25) for the whole period. The grids, where sea ice concentration is higher than 0.25, are treated as grids with missing H_s. So H_s trend values are present for a grid point when there is no missing H_s for the entire period.

3. Global Wave Height Trends for Different External Forcing in CMIP6

Figure 1 shows long-term trends in annual mean H_s from five-member ensemble mean as simulated by WW3_MRI-ESM2.0 during 1961–2020. The historical ALL simulation (Figure 1a) shows robust strengthening
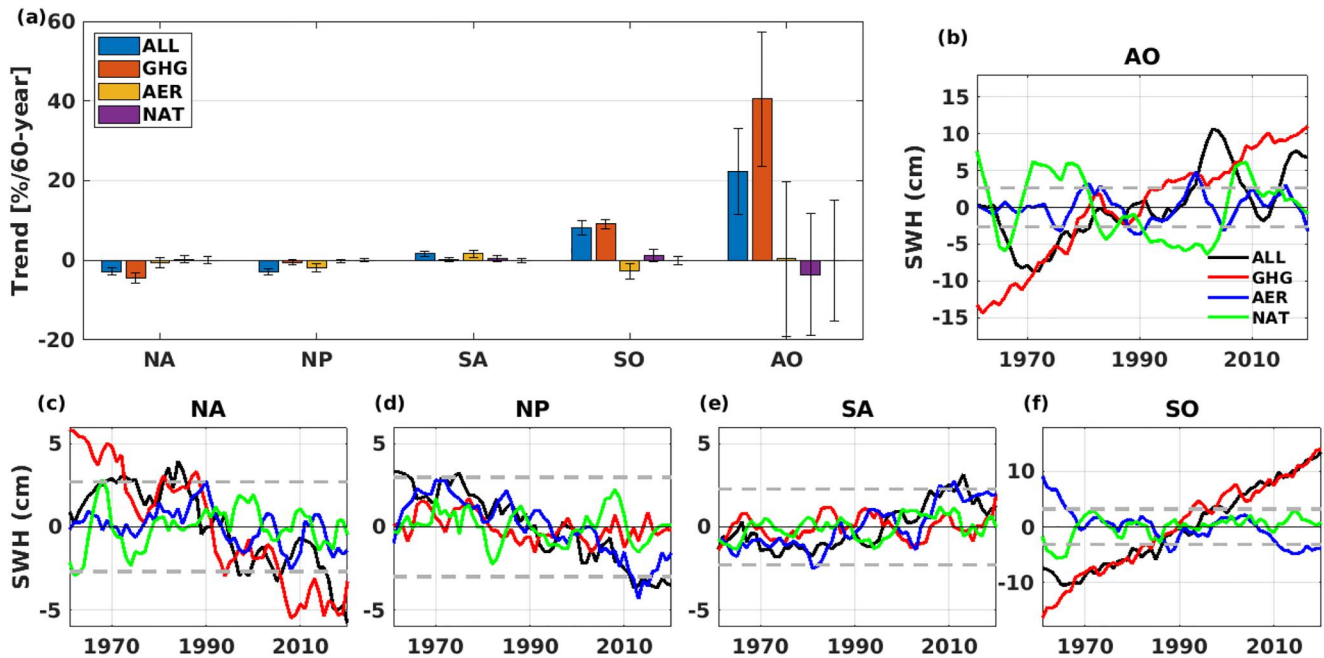
Figure 2. (a) Region (as in Figure 1a) averaged trends in H_s from WW3/MRI-ESM2.0 simulations during 1961–2020: five member mean (bar) and ±standard deviation (error bar). The rightmost vertical whiskers indicate range of internal variability defined by CTL. (b–f) Time series of 5-year running mean of region averaged H_s for AO, NA, NP, SA, and SO respectively during 1961–2020. The gray lines indicate 5%–95% ranges of CTL simulations.

over the Arctic Ocean (AO), Southern Ocean (SO) and South Atlantic (SA) Ocean. The regions with robust weakening include the North Pacific (NP), North Atlantic (NA) and some parts of North Indian Ocean. GHG results (Figure 1b) display similar patterns to ALL in many regions of global Ocean (except South Atlantic), suggesting strong GHG influence on total H_s trends. AER explains increasing H_s over SA and decreasing H_s over NP. Specifically, statistically robust AER trends (Figure 1c) exhibit opposite nature to GHG. It is consistent with positive forcings from greenhouse gases and negative forcings from total aerosol to total anthropogenic net effective radiative forcing (ERF) in MRI-ESM2.0 (Oshima et al., 2020). NAT trends (Figure 1d) are weak and not robust over the global ocean. Furthermore, seasonal mean H_s trends (Figure S1 in Supporting Information S1) are able to thoroughly reproduce the above spatial pattern and sign of trends for different forcing scenario. The influence of GHG and AER on the regions shown in boxes in Figure 1a are also clearly visible in seasonal trends (Figure S1 in Supporting Information S1).

Other CMIP6-based wave height simulations (Table S1 in Supporting Information S1) exhibit fairly similar H_s trends (Figures 1e–1g) as MRI-ESM2.0 based results (Figure 1a) during 1961–2020, further increasing the confidence in the wave simulations used in this study. The statistically significant downward trends in NA and NP and upward trends in AO, SO, and SA are found in WW3/ACCESS-CM2, WW3/EC-Earth3, and MASNUM-WAM/FIO-ESM v2.0, although using only single ensemble member. Yet, some differences exist between the different approaches. In particular, stronger negative values are seen in Northern Hemisphere (NH) in WW3/EC-Earth3 and stronger positive values for Southern Hemisphere (SH) in MASNUM-WAM/FIO-ESM v2.0. Overall, comparison between the three wave data sets are reasonable given the existing inter-model differences (Meucci et al., 2023). We acknowledge that dynamically coupled wave model and GCM data set are not yet available extensively, expect MASNUM-WAM/FIO-ESM v2.0. Therefore, advantage of ensembles of wave coupled GCMs (to standalone wave model) could not be quantified. It is worth mentioning that partly spurious positive H_s trends (figure not shown) are seen in ERA5 reanalysis (Hersbach et al., 2020) data set during 1961–2020 period, which can be associated with the discontinuities in the assimilated observations (Meucci et al., 2023). Nevertheless, satellite altimeter measurements are not available for such long period to compare 60-year trends, although reasonable comparison with MRI-ESM2.0 based H_s trends are reported previously (Patra et al., 2023b).

Figure 2a shows the regionally-averaged results for AO, NA, NP, SA, and SO, which are the regions having experienced the largest changes. The historical-ALL (externally forced) trends are larger than internal variability

range for all the ocean basins shown in the figure. Moreover, anthropogenic forcings (GHG and AER) are found to be responsible for the total trends during 1961–2020 over the basins. Indeed, the response of NAT forcing is small everywhere. To describe the relative dominance of GHG and AER, GHG dominates over AO, SO and NA; whereas AER over NP and SA. The polar seas show exceptional increment like none other basins. The 60-year trend in ALL simulation over NA, NP and SA are within 3%, but, in SO and AO it is around 8.2% and 22.3%, respectively. The GHG, AER, and NAT induced trends are 9.1%($\pm$1.1%) −2.7%($\pm$1.9%) 1.2%($\pm$1.6%) respectively for SO, and 40.5%($\pm$16.8%), 0.4%($\pm$19.3%), −3.5%($\pm$15.3%) for the AO basin. The inter-member standard deviation is quite large for AER and NAT signal over the AO basin, additionally, CTL variability is also quite considerable, though lesser than ALL signal. The difference between ALL and linear sum (GHG + AER + NAT) can arise due to nonlinear interaction between the forcings (J. Deng et al., 2020; Oshima et al., 2020) or response to land use forcing (Andrews et al., 2017).

Figures 2b–2f show time-series of H_s anomalies for the different external forcings, as well as the range of CTL simulations. The time-series for ALL simulation exceeds the CTL range (gray lines, 5%–95%), indicating a robust change. For the AO (Figure 2b), the external forcings are beyond the range of internal fluctuation, moreover monotonic rise in GHG H_s signal induces increase in historical H_s. Similar findings can be seen for the SO (Figure 2f), stronger monotonic rise in GHG H_s and a weaker fall in AER H_s signal cause rise in total (ALL) wave height. However, for NA, NP and SA, some of the forcings are within the range of internal fluctuation, although ALL forcing is the clear exception. In agreement with higher percentage change, higher anomalies are found for polar seas. For the NA, GHG signal exceeds the CTL ranges and the dominating forcing to total H_s decrease. In contrast, AER is the robust signal as well as the dominating one for NP and SA. Overall, anthropogenic signals are found to be robust and the driving factors for total changes for all the basins discussed here.

4. Global Trends in Wind Speed in CMIP6 and DAMIP Experiments

The ensemble mean wind speed from MRI-ESM2.0 (Figure 3) shows quite consistent pattern of trends with that of H_s (Figures 1a–1d). The ALL simulation generally shows negative trends over NH, including the NA and NP, with exception over the Arctic region. Moreover, significant positive trends are seen in the SH subtropics and surrounding SO regions, similar with the findings of K. Deng et al. (2021). GHG forcing exhibits high level of agreement with the ALL forcing, with negative trends over the NA and NP, and positive trends over the AO and SO. Noteworthy influence of AER on total H_s trends can be seen over the NP and SA regions. In contrast, NAT signal shows weak and insignificant changes over most regions. The inference from the above analysis is that the anthropogenic forcing (GHG and AER) can be attributed to surface wind speed changes during 1961–2020.

To address the single model limitation issue, the CMIP6 multi model mean (MMM) results are compared with MRI-ESM2.0. The MMM results (Figure 3) agree with MRI-ESM2.0 on spatial distribution and sign of trends, although the MMM shows stronger positive trends than the latter. The GHG dominance is clearly evident on total wind speed trends, not to mention the AO, SO and NA. In general, the wind speed associated with AER has weakened over the analysis period, including the NP. Consistent with above analyses, weak trends are present for NAT simulations. Overall, the MMM results agree with MRI-ESM2.0 for attribution of anthropogenic forcing and signs of the trends. Here, we acknowledge the underestimation of positive trends in GHG and ALL simulations from MRI-ESM2.0 with respect to MMM, which does not include MRI-ESM2.0. The multi-member ensemble mean for each of these individual climate models (Figure S2 in Supporting Information S1) show agreement in spatial distribution and sign of trends with MRI-ESM2.0, but produce higher magnitude for trends. One should note the low spatial (Table S2 in Supporting Information S1) and temporal resolution (1 day) of these models with compared to MRI-ESM2.0 (1.125° × 1.11209°–1.12148° and 3 hourly).

5. Driving Mechanisms of Wave Height Changes Over the Arctic and Antarctic Polar Oceans

Since polar seas are shown to have experienced the largest wave height changes over the 1961–2020 period, and since polar wave climate is known to be affected by changes in sea ice extent (Thomson & Rogers, 2014), we focus on the possible drivers over these regions during the months of minimum sea ice extent (September for NH and March for SH) utilizing the MRI-ESM2.0 data set. With the global warming, reduction in sea ice extent
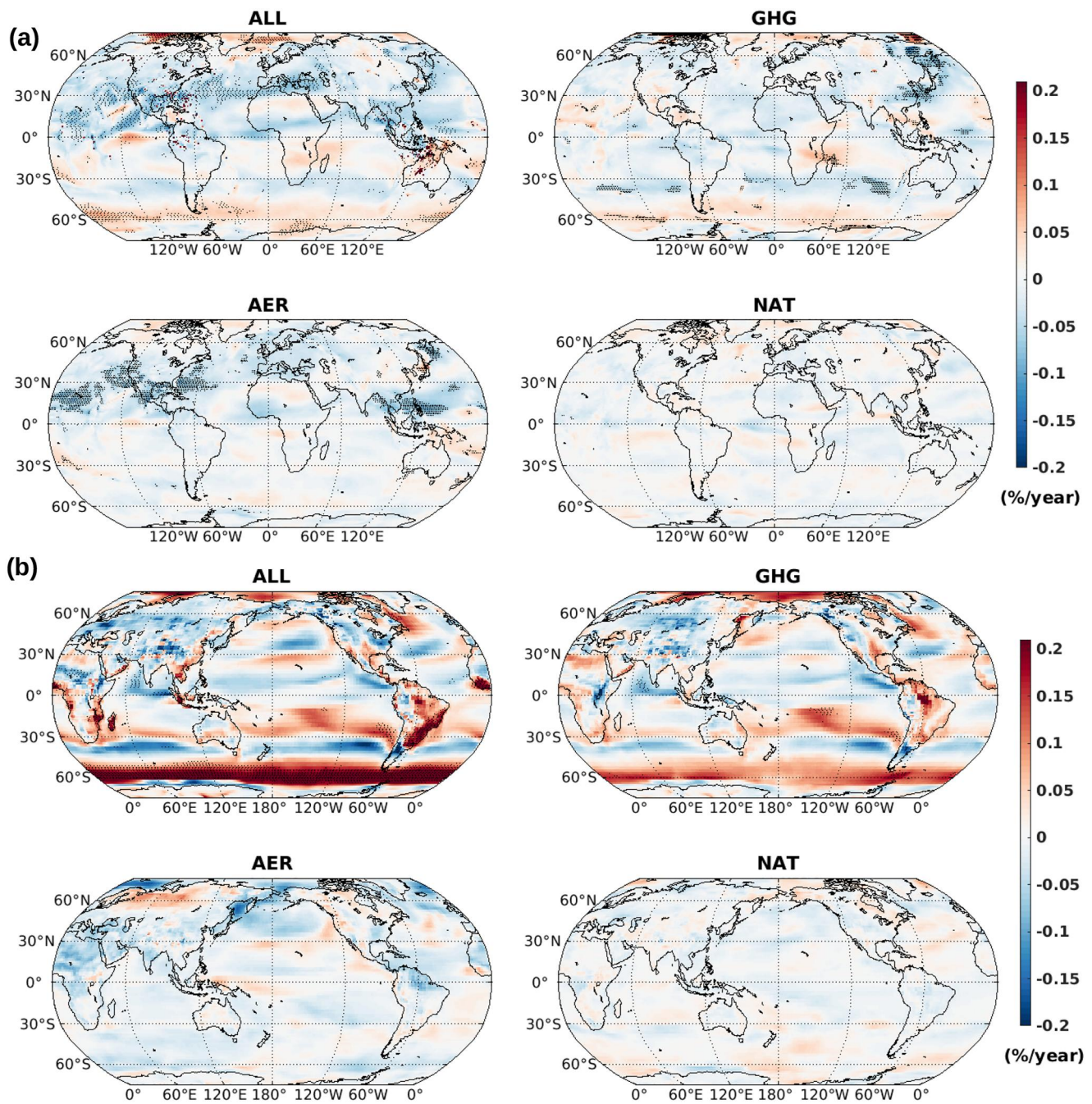
Figure 3. Linear trend (%) expressed as percentage change per year during 1961–2020 for annual mean surface wind speed from MRI-ESM2.0 simulations for ALL, GHG, AER, NAT forcing scenario (5 member mean) (a). Same analysis but using multi model mean (MMM) derived from 3 CMIP6 models having 36 ensemble member in total for ALL, and 35 for the others (b). The percentage is calculated with respect to 1961–2020 climatology. Robustness is defined at grids (stippling) considering both inter-annual and inter-member variability.

increases available fetch for waves in these basins. Although MRI-ESM2.0 has bit smaller September sea ice extents than the observation by Walsh et al. (2017), the decadal-to-multidecadal variations agree well between the model simulation and the observation (Aizawa et al., 2021). Moreover, MRI-ESM2.0 has been reported as one of the few CMIP6 models which are able to simulate a plausible amount of sea ice loss and simultaneously a plausible change in global mean temperature over time compared to the observational estimate (Notz & Community, 2020). Although CMIP6 models have larger intermodel spread for Antarctic Sea ice area than that in the Arctic, moderately higher confidence is reported in simulation of Antarctic climate in CMIP6 than previous

generations (Roach et al., 2020) of CMIPs. To further substantiate the sea ice area in Antarctic, 1979–2014 mean sea ice area and concentration in February from MRI-ESM2.0 appear to be close to observation (Roach et al., 2020). Moreover, the sea-ice edge distribution of the Antarctic simulated by MRI-ESM2.0 is consistent with observations (Yukimoto et al., 2019).

MRI-ESM2.0 simulates consistent decline in NH sea ice extent over 1961–2020 period. The end of both summer and winter months (March and September) show decline, but with faster decline in September in NH (Figure S3 in Supporting Information S1). Whereas in SH both March and September exhibit almost similar level of decline (Figure S3 in Supporting Information S1). September changes between 2001–2020 and 1961–1980 over the Arctic Ocean shows statistically significant decline in sea ice area fraction (Figure 4a), in line with Arctic warming. The strong decline associated with GHG forcing is the major factor for the sea ice depletion over the Arctic. In addition, weaker decline, although statistically significant can be seen in connection with AER and NAT influence, but only limited to the Pacific sector, especially in the regions of the Chukchi and East Siberian seas.

The change pattern for wind speed indicates intensification in the recent decades for north of 70°N in Pacific sector (Chukchi, East Siberian and Laptev sea). In the further north (>80°N), the significant increase cover eastern Arctic Ocean. It seems that positive changes of GHG and NAT have induced the wind speed increment for the polar region (>70°N). There might be some traces of internal variability as we use 20-year mean in the analysis.

Finally, for wave height, strong increase is experienced over the entire circle north of 70°N (Figure 4a), this being the region where sea ice edge shifted northward as a result of ice melting. The H_s increases are reflected over wider areas in Barents-Kara seas, northern Greenland sea, and bit less wider areas of Chukchi, East Siberian and Laptev sea, also bit scattered over Beaufort sea and Baffin Bay. For the GHG simulation, these increases are even stronger and extend further northward. In contrast, weaker changes are present for AER and NAT simulations. In addition, larger fetch is clear in case of GHG than AER and NAT simulations, as a result of more northward sea ice retreat associated with GHG forcings. Overall, wave height increase is majorly associated with increase of the effective fetch (less ice cover) along with wind speed increase too. Besides, there is a clear signature of the sea ice variability in H_s change patterns. In line with this analysis, Liu et al. (2016) reported wave height increase over the Arctic despite decrease in wind speed during 2007–2015. Sea ice retreat majorly contributes to the variability of waves in the Arctic Shelf seas (Khon et al., 2014; Wang et al., 2015). It should be noted that, in the Atlantic sector, local winds and remotely generated swell combine together to determine changes of sea state (Semedo et al., 2015). Nonetheless, positive feedback between sea-ice area decline and wind speed increase is reported by Alkama et al. (2020), which is very clear for March over the Arctic (Figure S4 in Supporting Information S1). The regions (Barents and northern Greenland sea) with strong decline in sea ice coincide with the regions with wind speed increase and H_s increase. As in September, GHG emerges as the most controlling factor in March, but strong changes appears bit southward.

For the Antarctic region, the sea ice changes during March implies decline in sea ice area concentration around the Antarctic coastline, over much wider areas in west Antarctic (Figure 4b). Consistent sea ice decline persist for the case of GHG. Contrary to this, increases in sea ice extent appear for AER simulations. And, weaker signal is present for NAT simulations. Overall, GHG forcing is found to contribute dominantly to the sea ice deline in MRI-ESM2.0.

Statistically significant wind speed increment can be seen around Southern Ocean basin in ALL simulations, mostly associated with GHG induced increase. Although these wind speed increase are not continuously present around the Antarctic coastlines, strong significant wave height increase appears all over the Antarctic seas (Figure 4b), specifically over larger areas in west Antarctic seas. This pattern of increment is mostly induced by GHG forcing. Scattered negative (weak) changes are present for AER (NAT) simulation. Similar to Arctic ocean, larger fetch becomes available for waves to grow in GHG scenario, in contrast to AER and NAT. The qualitative contribution of wind speed to wave height increase is higher for Antarctic seas than the Arctic. In addition, reduction in sea ice can induce increase in surface wind in Arctic and Antarctic seas (Alkama et al., 2020; Iwasaki, 2023; Khon et al., 2014). Thus sea ice is majorly responsible for the increase wave power over the polar seas (Iwasaki, 2023).
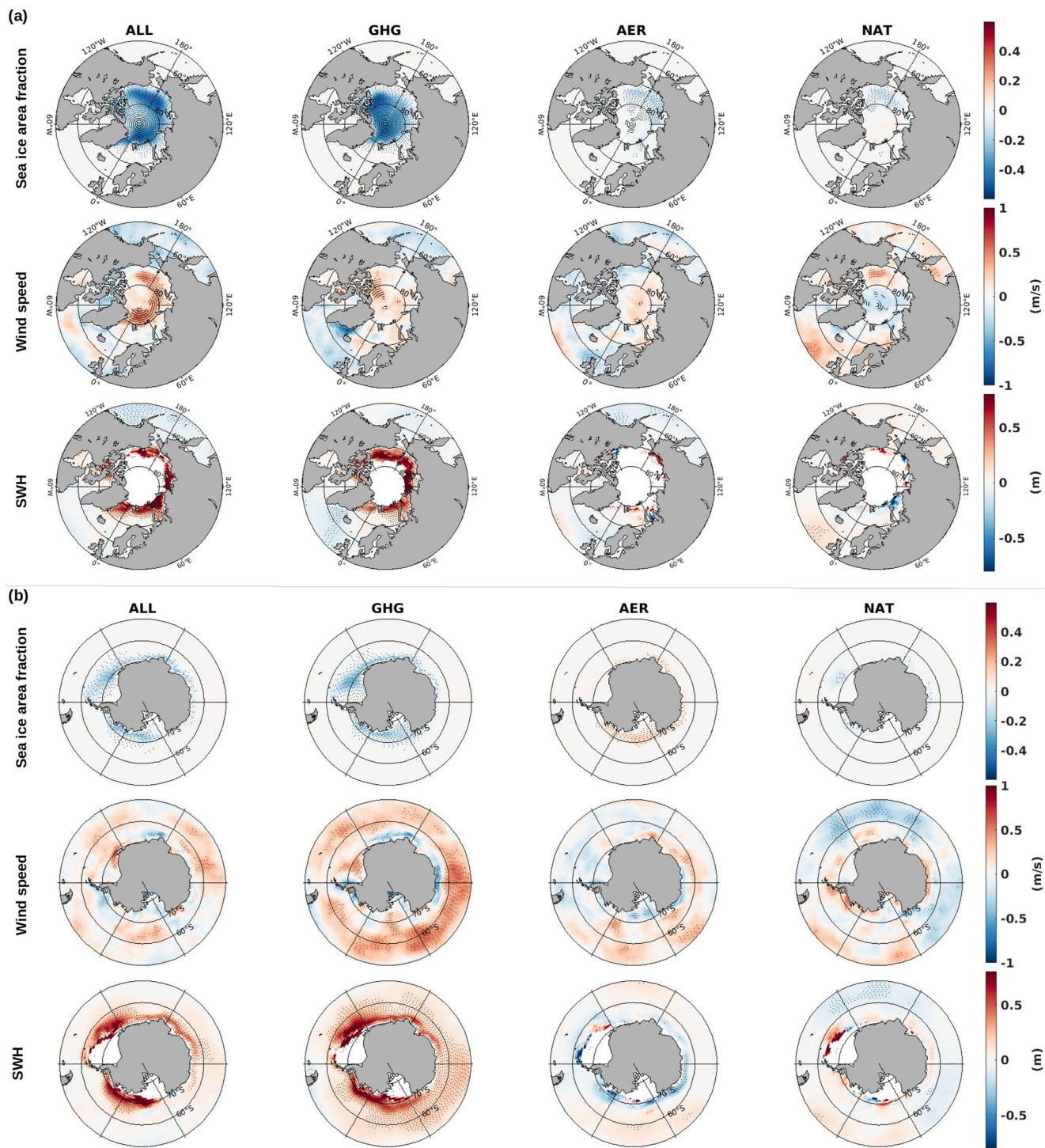
Figure 4. (a) September Arctic Ocean changes between (2001–2020) and (1961–1980) using ensemble mean values in MRI-ESM2.0 based simulations. Statistical significance (stippling) is following *t*-test using 5 members × 20 years = 100 data for each period. Changes over the Antarctic Ocean are shown for the month of March (b).

6. Conclusion

We conducted DAMIP experiments using MRI-ESM2.0 based simulations and identified the external forcings responsible for historical wave height changes during the 1961–2020 period. Historical-ALL simulations, based on MRI-ESM2.0 and other CMIP6 models, have undergone robust strengthening over the Arctic Ocean, Southern

Ocean, and South Atlantic, but weakening over the North Pacific and North Atlantic. The DAMIP experiments suggest that historical H_s changes are mostly driven by anthropogenic (GHG and AER) effects alone, additionally GHG dominates over AER in most basins except NP and SA. The surface wind speed corroborates the above changes in MRI-ESM2.0 and in multi model mean as well.

We further quantified the role of sea ice and surface winds to historical H_s changes over the Arctic and Antarctic regions involving DAMIP experiments. The sea ice decline appears to be a more important contributor to H_s increase over the Arctic, which can be further explained by GHG-induced ice depletion. Moreover, GHG instigate poleward sea ice retreat to a greater extent (longer fetch) than the other factors. The influence of surface winds is more influential in Antarctic H_s increase than that of Arctic. GHG signal emerges as the controlling factor for both sea ice decline and wind intensification, which further reflect in H_s rise.

Overall, the DAMIP multimodel analyses showed that anthropogenic forcings are mostly responsible for the historical changes in wave height. The amplification of wave height in the Polar seas are remarkable, which can cause more sea ice breaks, and subsequently accelerates ice melting (Boutin et al., 2020; Thomson & Rogers, 2014). We acknowledge the non-availability of any other H_s data in the framework of DAMIP. The detection and attribution of H_s trends to anthropogenic and natural causes using multi models and large ensembles, when available, would be more robust. Moreover the attribution results are based on five-ensemble member, it would be ideal to use at least 10 members (Casas-Prat et al., 2022) in order to be more confident in conclusions.

Data Availability Statement

The DAMIP data used in this study are available on the Earth System Grid Federation (ESGF) website (Stockhause & Lautenschlager, 2017). Wave simulations used in the study are from Patra et al. (2023a), CSIRO Data: (Meucci et al., 2021), and FIO data: (Song et al., 2020b).

References

Aizawa, T., Ishii, M., Oshima, N., Yukimoto, S., & Hasumi, H. (2021). Arctic warming and associated sea ice reduction in the early 20th century induced by natural forcings in MRI-ESM2.0 climate simulations and multimodel analyses. *Geophysical Research Letters*, *48*(8), e2020GL092336. https://doi.org/10.1029/2020GL092336

Alkama, R., Koffi, E. N., Vavrus, S. J., Diehl, T., Francis, J. A., Stroeve, J., et al. (2020). Wind amplifies the polar sea ice retreat. *Environmental Research Letters*, *15*(12), 124022. https://doi.org/10.1088/1748-9326/abc379

Andrews, T., Betts, R. A., Booth, B. B. B., Jones, C. D., & Jones, G. S. (2017). Effective radiative forcing from historical land use change. *Climate Dynamics*, *48*(11), 3489–3505. https://doi.org/10.1007/s00382-016-3280-7

Bi, D., Dix, M., Marsland, S., O'Farrell, S., Sullivan, A., Bodman, R., et al. (2020). Configuration and spin-up of ACCESS-CM2, the new generation Australian Community Climate and Earth System Simulator Coupled Model. *Journal of Southern Hemisphere Earth Systems Science*, *70*(1), 225–251. https://doi.org/10.1071/ES19040

Bindoff, N. L., Stott, P. A., AchutaRao, K. M., Allen, M. R., Gillett, N., Gutzler, D., et al. (2013). Detection and attribution of climate change: From global to regional. In T. F. Stocker, et al. (Eds.), *Climate change 2013: The physical science basis. Contribution of working group I to the fifth assessment report of the intergovernmental panel on climate change* (pp. 867–952). Cambridge University Press. https://doi.org/10.1017/CBO9781107415324.022

Boucher, O., Denvil, S., Levavasseur, G., Cozic, A., Caubel, A., Foujols, M.-A., et al. (2018). *IPSL IPSL-CM6A-LR model output prepared for CMIP6 CMIP*. Earth System Grid Federation. https://doi.org/10.22033/ESGF/CMIP6.1534

Boutin, G., Lique, C., Ardhuin, F., Rousset, C., Talandier, C., Accensi, M., & Girard-Ardhuin, F. (2020). Towards a coupled model to investigate wave–sea ice interactions in the Arctic marginal ice zone. *The Cryosphere*, *14*(2), 709–735. https://doi.org/10.5194/tc-14-709-2020

Casas-Prat, M., Hemer, M. A., Dodet, G., Morim, J., Wang, X. L., Mori, N., et al. (2024). Wind-wave climate changes and their impacts. *Nature Reviews Earth & Environment*, *5*(1), 23–42. https://doi.org/10.1038/s43017-023-00502-0

Casas-Prat, M., Wang, X. L., Mori, N., Feng, Y., Chan, R., & Shimura, T. (2022). Effects of internal climate variability on historical ocean wave height trend assessment. *Frontiers in Marine Science*, *9*. https://doi.org/10.3389/fmars.2022.847017

Cavaleri, L., Fox-Kemper, B., & Hemer, M. (2012). Wind waves in the coupled climate system. *Bulletin of the American Meteorological Society*, *93*(11), 1651–1661. https://doi.org/10.1175/BAMS-D-11-00170.1

Chen, S., Qiao, F., Jiang, W., Guo, J., & Dai, D. (2019). Impact of surface waves on wind stress under low to moderate wind conditions. *Journal of Physical Oceanography*, *49*(8), 2017–2028. https://doi.org/10.1175/JPO-D-18-0266.1

Deike, L. (2022). Mass transfer at the ocean–atmosphere interface: The role of wave breaking, droplets, and bubbles. *Annual Review of Fluid Mechanics*, *54*(1), 191–224. https://doi.org/10.1146/annurev-fluid-030121-014132

Deng, J., Dai, A., & Xu, H. (2020). Nonlinear climate responses to increasing CO_2 and anthropogenic aerosols simulated by CESM1. *Journal of Climate*, *33*(1), 281–301. https://doi.org/10.1175/JCLI-D-19-0195.1

Deng, K., Azorin-Molina, C., Minola, L., Zhang, G., & Chen, D. (2021). Global near-surface wind speed changes over the last decades revealed by reanalyses and CMIP6 model simulations. *Journal of Climate*, *34*(6), 2219–2234. https://doi.org/10.1175/JCLI-D-20-0310.1

Deser, C., Phillips, A., Bourdette, V., & Teng, H. (2012). Uncertainty in climate change projections: The role of internal variability. *Climate Dynamics*, *38*(3), 527–546. https://doi.org/10.1007/s00382-010-0977-x

Dobrynin, M., Murawski, J., Baehr, J., & Ilyina, T. (2015). Detection and attribution of climate change signal in ocean wind waves. *Journal of Climate*, *28*(4), 1578–1591. https://doi.org/10.1175/JCLI-D-13-00664.1

Döscher, R., Acosta, M., Alessandri, A., Anthoni, P., Arsouze, T., Bergman, T., et al. (2022). The EC-Earth3 Earth system model for the Coupled Model Intercomparison Project 6. *Geoscientific Model Development*, *15*(7), 2973–3020. https://doi.org/10.5194/gmd-15-2973-2022

Erikson, L., Morim, J., Hemer, M., Young, I., Wang, X. L., Mentaschi, L., et al. (2022). Global ocean wave fields show consistent regional trends between 1980 and 2014 in a multi-product ensemble. *Communications Earth & Environment*, *3*(1), 320. https://doi.org/10.1038/s43247-022-00654-9

Eyring, V., Bony, S., Meehl, G. A., Senior, C. A., Stevens, B., Stouffer, R. J., & Taylor, K. E. (2016). Overview of the Coupled Model Intercomparison Project Phase 6 (CMIP6) experimental design and organization. *Geoscientific Model Development*, *9*(5), 1937–1958. https://doi.org/10.5194/gmd-9-1937-2016

Gillett, N. P., Kirchmeier-Young, M., Ribes, A., Shiogama, H., Hegerl, G. C., Knutti, R., et al. (2021). Constraining human contributions to observed warming since the pre-industrial period. *Nature Climate Change*, *11*(3), 207–212. https://doi.org/10.1038/s41558-020-00965-9

Gillett, N. P., Shiogama, H., Funke, B., Hegerl, G., Knutti, R., Matthes, K., et al. (2016). The detection and attribution model intercomparison project (DAMIP v1.0) contribution to CMIP6. *Geoscientific Model Development*, *9*(10), 3685–3697. https://doi.org/10.5194/gmd-9-3685-2016

Hasselmann, K. (1993). Optimal fingerprints for the detection of time-dependent climate change. *Journal of Climate*, *6*(10), 1957–1971. https://doi.org/10.1175/1520-0442(1993)006⟨1957:OFFTDO⟩2.0.CO;2

Hersbach, H., Bell, B., Berrisford, P., Hirahara, S., Horányi, A., Muñoz-Sabater, J., et al. (2020). The ERA5 global reanalysis. *Quarterly Journal of the Royal Meteorological Society*, *146*(730), 1999–2049. https://doi.org/10.1002/qj.3803

Hochet, A., Dodet, G., Sévellec, F., Bouin, M.-N., Patra, A., & Ardhuin, F. (2023). Time of emergence for altimetry-based significant wave height changes in the North Atlantic. *Geophysical Research Letters*, *50*(9), e2022GL102348. https://doi.org/10.1029/2022GL102348

Iwasaki, S. (2023). Increase in the wave power caused by decreasing sea ice over the Sea of Okhotsk in winter. *Scientific Reports*, *13*(1), 2539. https://doi.org/10.1038/s41598-023-29692-9

Khon, V. C., Mokhov, I. I., Pogarskiy, F. A., Babanin, A., Dethloff, K., Rinke, A., & Matthes, H. (2014). Wave heights in the 21st century Arctic Ocean simulated with a regional climate model. *Geophysical Research Letters*, *41*(8), 2956–2961. https://doi.org/10.1002/2014GL059847

Liu, Q., Babanin, A. V., Zieger, S., Young, I. R., & Guan, C. (2016). Wind and wave climate in the arctic ocean as observed by altimeters. *Journal of Climate*, *29*(22), 7957–7975. https://doi.org/10.1175/JCLI-D-16-0219.1

Masson-Delmotte, V., Zhai, P., Pirani, A., Connors, C., Péan, C., Berger, S., et al. (2021). In *Climate change 2021: The physical science basis. Contribution of working group I to the sixth assessment report of the intergovernmental panel on climate change*. Cambridge University Press.

Meucci, A., Young, I., Hemer, M., & Trenham, C. (2021). CMIP6 global wind-wave 21st century climate projections phase 1. v13. Service collection [Dataset]. *CSIRO*. http://hdl.handle.net/102.100.100/432508?index=1

Meucci, A., Young, I. R., Hemer, M., Trenham, C., & Watterson, I. G. (2023). 140 years of global ocean wind-wave climate derived from CMIP6 ACCESS-CM2 and EC-Earth3 GCMs: Global trends, regional changes, and future projections. *Journal of Climate*, *36*(6), 1605–1631. https://doi.org/10.1175/JCLI-D-21-0929.1

Morim, J., Hemer, M., Wang, X. L., Cartwright, N., Trenham, C., Semedo, A., et al. (2019). Robustness and uncertainties in global multivariate wind-wave climate projections. *Nature Climate Change*, *9*(9), 711–718. https://doi.org/10.1038/s41558-019-0542-5

Notz, D., & Community, S. (2020). Arctic Sea ice in CMIP6. *Geophysical Research Letters*, *47*(10), e2019GL086749. https://doi.org/10.1029/2019GL086749

Oshima, N., Yukimoto, S., Deushi, M., Koshiro, T., Kawai, H., Tanaka, T. Y., & Yoshida, K. (2020). Global and Arctic effective radiative forcing of anthropogenic gases and aerosols in MRI-ESM2.0. *Progress in Earth and Planetary Science*, *7*(1), 38. https://doi.org/10.1186/s40645-020-00348-w

Patra, A., Dodet, G., & Accensi, M. (2023a). Glob1d_cmip6.ifremer [Dataset]. *CMIP*. https://doi.org/10.12770/0983962b-4acc-4f8f-9484-e2195029b87b

Patra, A., Dodet, G., & Accensi, M. (2023b). Historical global ocean wave data simulated with CMIP6 anthropogenic and natural forcings. *Scientific Data*, *10*(1), 325. https://doi.org/10.1038/s41597-023-02228-6

Roach, L. A., Dörr, J., Holmes, C. R., Massonnet, F., Blockley, E. W., Notz, D., et al. (2020). Antarctic Sea ice area in CMIP6. *Geophysical Research Letters*, *47*(9), e2019GL086729. https://doi.org/10.1029/2019GL086729

Semedo, A., Vettor, R., Breivik, O., Sterl, A., Reistad, M., Soares, C. G., & Lima, D. (2015). The wind sea and swell waves climate in the Nordic seas. *Ocean Dynamics*, *65*(2), 223–240. https://doi.org/10.1007/s10236-014-0788-4

Seong, M.-G., Min, S.-K., Kim, Y.-H., Zhang, X., & Sun, Y. (2021). Anthropogenic greenhouse gas and aerosol contributions to extreme temperature changes during 1951–2015. *Journal of Climate*, *34*(3), 857–870. https://doi.org/10.1175/JCLI-D-19-1023.1

Song, Z., Bao, Y., Zhang, D., Shu, Q., Song, Y., & Qiao, F. (2020a). Centuries of monthly and 3-hourly global ocean wave data for past, present, and future climate research. *Scientific Data*, *7*(1), 226. https://doi.org/10.1038/s41597-020-0566-8

Song, Z., Bao, Y., Zhang, D., Shu, Q., Song, Y., & Qiao, F. (2020b). Simulated long-term monthly ocean surface waves parameters from fio-esm v2.0 cmip6 experiments for past, present, and future climate research [Dataset]. *Figshare*. https://doi.org/10.6084/m9.figshare.c.4819503.v1

Stockhause, M., & Lautenschlager, M. (2017). Cmip6 data citation of evolving data [Dataset]. *Data Science Journal*, *16*. https://doi.org/10.5334/dsj-2017-030

Swart, N. C., Cole, J. N. S., Kharin, V. V., Lazare, M., Scinocca, J. F., Gillett, N. P., et al. (2019). The Canadian Earth System Model version 5 (CanESM5.0.3). *Geoscientific Model Development*, *12*(11), 4823–4873. https://doi.org/10.5194/gmd-12-4823-2019

Taylor, K. E., Stouffer, R. J., & Meehl, G. A. (2012). An overview of CMIP5 and the experiment design. *Bulletin of the American Meteorological Society*, *93*(4), 485–498. https://doi.org/10.1175/BAMS-D-11-00094.1

Thomson, J., & Rogers, W. E. (2014). Swell and sea in the emerging Arctic Ocean. *Geophysical Research Letters*, *41*(9), 3136–3140. https://doi.org/10.1002/2014GL059983

Timmermans, B. W., Gommenginger, C. P., Dodet, G., & Bidlot, J.-R. (2020). Global wave height trends and variability from new multimission satellite altimeter products, reanalyses, and wave buoys. *Geophysical Research Letters*, *47*(9), e2019GL086880. https://doi.org/10.1029/2019GL086880

Toffoli, A., McConochie, J., Ghantous, M., Loffredo, L., & Babanin, A. V. (2012). The effect of wave-induced turbulence on the ocean mixed layer during tropical cyclones: Field observations on the Australian North-West Shelf. *Journal of Geophysical Research*, *117*(C11), C00J24. https://doi.org/10.1029/2011JC007780

Voldoire, A., Saint-Martin, D., Sénési, S., Decharme, B., Alias, A., Chevallier, M., et al. (2019). Evaluation of CMIP6 DECK experiments with CNRM-CM6-1. *Journal of Advances in Modeling Earth Systems*, *11*(7), 2177–2213. https://doi.org/10.1029/2019MS001683

Walsh, J. E., Fetterer, F., Scott stewart, J., & Chapman, W. L. (2017). A database for depicting Arctic sea ice variations back to 1850. *Geographical Review*, *107*(1), 89–107. https://doi.org/10.1111/j.1931-0846.2016.12195.x

Wang, X. L., Feng, Y., Swail, V. R., & Cox, A. (2015). Historical changes in the Beaufort–Chukchi–Bering seas surface winds and waves, 1971–2013. *Journal of Climate*, *28*(19), 7457–7469. https://doi.org/10.1175/JCLI-D-15-0190.1

Young, I. R., & Ribal, A. (2019). Multiplatform evaluation of global trends in wind speed and wave height. *Science*, *364*(6440), 548–552. https://doi.org/10.1126/science.aav9527

Yukimoto, S., Kawai, H., Koshiro, T., Oshima, N., Yoshida, K., Urakawa, S., et al. (2019). The Meteorological Research Institute Earth System Model Version 2.0, MRI-ESM2.0: Description and basic evaluation of the physical component. *Journal of the Meteorological Society of Japan. Ser. II*, *97*(5), 931–965. https://doi.org/10.2151/jmsj.2019-051